

pubs.acs.org/JPCB Article

# Enhancing Nanoparticle Detection in Interferometric Scattering (iSCAT) Microscopy Using a Mask R-CNN

Michael J. Boyle, Yale E. Goldman, and Russell J. Composto\*



Cite This: J. Phys. Chem. B 2023, 127, 3737-3745



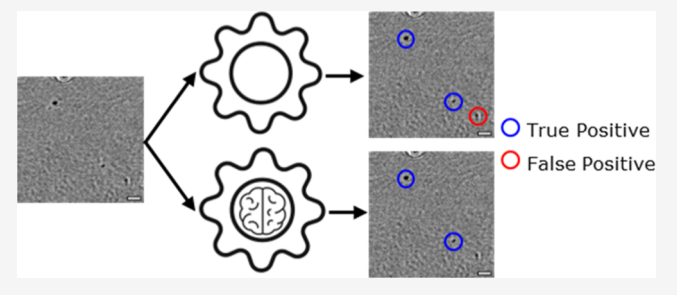
**ACCESS** I

III Metrics & More

Article Recommendations

s Supporting Information

ABSTRACT: Interferometric scattering microscopy (iSCAT) is a label-free optical microscopy technique that enables imaging of individual nano-objects such as nanoparticles, viruses, and proteins. Essential to this technique is the suppression of background scattering and identification of signals from nano-objects. In the presence of substrates with high roughness, scattering heterogeneities in the background, when coupled with tiny stage movements, cause features in the background to be manifested in background-suppressed iSCAT images. Traditional computer vision algorithms detect these background features as particles,



limiting the accuracy of object detection in iSCAT experiments. Here, we present a pathway to improve particle detection in such situations using supervised machine learning via a mask region-based convolutional neural network (mask R-CNN). Using a model iSCAT experiment of 19.2 nm gold nanoparticles adsorbing to a rough layer-by-layer polyelectrolyte film, we develop a method to generate labeled datasets using experimental background images and simulated particle signals and train the mask R-CNN using limited computational resources via transfer learning. We then compare the performance of the mask R-CNN trained with and without inclusion of experimental backgrounds in the dataset against that of a traditional computer vision object detection algorithm, Haar-like feature detection, by analyzing data from the model experiment. Results demonstrate that including representative backgrounds in training datasets improved the mask R-CNN in differentiating between background and particle signals and elevated performance by markedly reducing false positives. The methodology for creating a labeled dataset with representative experimental backgrounds and simulated signals facilitates the application of machine learning in iSCAT experiments with strong background scattering and thus provides a useful workflow for future researchers to improve their image processing capabilities.

#### ■ INTRODUCTION

In the past two decades, <sup>1</sup> interferometric scattering (iSCAT) microscopy has enabled imaging and tracking of nano-objects such as gold nanoparticles, <sup>2–5</sup> viruses, <sup>6</sup> and individual proteins <sup>7–9</sup> for dynamic studies on cell membranes, <sup>5</sup> molecular motors, <sup>10</sup> and quantitative mass/size measurements. <sup>11–13</sup> As a scattering-based technique, imaging of nano-objects in iSCAT experiments does not require fluorescent labeling. <sup>14</sup> This advantage mitigates challenges inherent to fluorescence-based techniques such as photobleaching and photoblinking. <sup>14</sup> Fluorescent labels on the surfaces of nano-objects also alter their surface chemistry, rendering iSCAT advantageous in studies where surface chemistry dominates (e.g., adsorption experiments, interactions within a cell, and diffusion along surfaces). Given these advantages, the contributions of iSCAT to the biological and physical science community are continually growing.

The label-free capabilities of iSCAT also represent its greatest limitation. <sup>15</sup> All materials with a different refractive index than that of the surrounding medium will scatter light and convolute signals of interest with the background. Consequently, extracting meaningful information from iSCAT images is a two-step process: (1) identifying and

suppressing the background and (2) detecting objects of interest in background-suppressed images. While numerous background extraction and suppression techniques have been developed through optical enhancements <sup>12,16,17</sup> and software algorithms, <sup>8,12,14,18</sup> stage movements, on the order of tens of nanometers (comparable to the pixel size in many iSCAT configurations), are difficult to eliminate and cause background features to appear even in background-suppressed images. <sup>15</sup> This problem is especially evident when the background contains regions of high roughness or refractive index heterogeneity and limits the ability of iSCAT to detect scatterers in complex environments. Here, background features that produce signals due to stage drift or vibrations appear as objects with a similar intensity and morphology as objects of interest in background-suppressed images. Experimenters are

Received: January 5, 2023 Revised: April 5, 2023 Published: April 19, 2023





typically required to perform time-consuming, intricate filtering of detections with similar characteristics. The method could therefore benefit from improvements in step two of the analysis process through improved computer vison strategies to detect particles in complex iSCAT images where less effort has been focused to date.

Convolutional neural networks (CNNs) in the field of supervised machine learning computer vision have emerged as a powerful means to improve performance in the problem of object detection in scientific images relative to traditional edge and thresholding computer vision algorithms. 19,20 Still, employing supervised machine learning in object detection currently requires a labeled dataset (i.e., known truths of object locations) that is representative of experimental images to use in training a CNN.<sup>21,22</sup> In a recent publication, Newby<sup>23</sup> et al. circumvented this limitation by generating a dataset consisting of synthetic fluorescent microscopy images by mathematically modeling both background and particle signals. However, in background-suppressed iSCAT images, the background is comparatively more complex and difficult to simulate. This makes creating simulated datasets to use in training a CNN for object identification in iSCAT images challenging. Compounding the problem, training CNNs from randomly initialized weights requires large datasets and great amounts of computing power.<sup>20</sup> To facilitate the use of machine learning in iSCAT object detection, both these obstacles are addressed in this work.

We demonstrate a machine learning workflow to improve object detection in complex background-suppressed iSCAT images. To accomplish this, we establish a procedure for creating labeled datasets containing synthetic particle signals with and without real experimental background-suppressed images from a model iSCAT experiment of 19.2 nm gold nanoparticles adsorbing to a rough layer-by-layer (LbL) polyelectrolyte film. We then train a mask region-based CNN (mask R-CNN)<sup>20,23</sup> in under 1 h using transfer learning<sup>24</sup> with readily accessible computational resources using the labeled datasets. By analyzing the model iSCAT experiment, we test the performance of the mask R-CNN (trained with and without experimental backgrounds in the dataset) in object detection and classification against that of a Haar-like feature image segmentation algorithm, an edge detection and threshold based algorithm previously used to detect objects in iSCAT images. 11,25 Results highlight the improved performance in object detection via a reduction of false positive (FP) detections [precision improved from 80.2% (Haar) to 96.5% (mask-RCNN)] and the importance of including representative experimental backgrounds in datasets. The result is not an automated, catch-all machine learning network to use in iSCAT image processing, but rather, it shows how to create datasets and optimize a CNN via transfer learning to improve object detection in experimental data. The improved analysis technique should expand capability of iSCAT to detect scattering objects in situations where background scattering is complex.

iSCAT Principles: Stage Movements Hinder Background Suppression. The theory behind iSCAT imaging has been reviewed extensively. We provide a summary of iSCAT operating principles below to highlight the benefit of enhanced object detection methods in expanding the application of iSCAT to substrates with strong scattering background features due to roughness and/or areas of varying refractive indexes.

The contrast in an iSCAT experiment is the result of interference between light scattered from nano-objects (e.g., nanoparticles, proteins, and viruses) and light from a reference source, commonly light reflected back at the substrate—solution interface from a normally incident coherent light source. The intensity of the signal detected is determined by the superposition of the scattered and reflected lights

$$I_{iSCAT} \propto |E_r + E_s|^2 = E_i^2 [r^2 + s^2 + 2r|s|\cos(\phi)]$$
 (1)

where  $I_{\rm iSCAT}$  is the intensity at the detector;  $E_v$   $E_{\rm S}$ , and  $E_{\rm i}$  are the reflected, scattered, and incident electric fields, respectively; r is the fraction of  $E_{\rm i}$  reflected; s is the fraction of  $E_{\rm i}$  scattered; and  $\phi$  is the phase difference between the reflected and scattered lights due to a difference in optical path length. According to Mie scattering theory (applicable when the wavelength of light is of the order of the nanoparticle size), the magnitude of s scales linearly with the volume of the particle  $(d_{\rm NP}^3)$ ,  $^{13,28}$  and in the limit of small scattering objects, reflected light dominates the detected signal making the pure scattering contribution negligible  $(r^2 \gg s^2)$ .  $^{28}$  eq 1 then reduces to

$$I_{\text{iSCAT}} = E_{\text{i}}^2 [r^2 + 2r | \text{slcos}(\phi)]$$
 (2)

Equation 2 illustrates the power of iSCAT and highlights its limitations. In comparison to pure scattering-based contrast techniques (i.e., dark field microscopy) where the scattering term for small objects decreases with the volume of the particle squared,<sup>28</sup> the scattering term in an iSCAT signal decreases linearly with the particle volume. This is what lowers the detection threshold for label-free imaging of nanoparticles, viruses, and individual proteins.<sup>9,11</sup> However, because all interfaces with a difference in the refractive index scatter light, backgrounds in iSCAT experiments often scatter light at stronger intensities than the nanoparticles or proteins of interest. To generate sufficient contrast,  $C_{iSCAT}$ , for analysis, strongly varying background features are typically suppressed by dividing or subtracting a reference background image from experimental images. This background suppression, the mechanisms of which are discussed in the Methods section, is described mathematically as

$$C_{\text{iSCAT}} = \frac{I_{\text{iSCAT}}}{I_{\text{bkg}}} = \frac{E_{\text{i}}^{2}[r_{\text{image}}^{2} + 2r_{\text{image}}|\text{slcos}(\phi)]}{E_{\text{i}}^{2}r_{\text{bkg}}^{2}}$$

$$\approx 1 - \frac{2|\text{slcos}(\phi)}{r}$$
(3)

where  $r_{\text{bkg}}$  represents the fraction of  $E_{\text{i}}$  reflected by the optics and substrate that forms the background reference from an earlier frame capture and  $r_{image}$  represents the fraction of  $E_i$ reflected that forms the image currently being analyzed. If the imaging stage and optical components are stable,  $r_{\rm bkg} = r_{\rm image}$ and all background reference features would be suppressed by division resulting in the approximate solution below eq 3. However, in practice, drift or vibrations on the order of tens of nanometers (i.e., comparable to the pixel dimension) are typical for optical microscopes. 15,29 These stage movements cause  $r_{\text{bkg}}$  to differ from  $r_{\text{image}}$ , and scattering from the substrate contributes significant features to background-suppressed images. These substrate features may have morphologies resembling those of scattering features from nano-objects, and the essential step of detecting objects of interest in background-suppressed iSCAT images becomes more difficult as background complexity increases. The challenges presented by

the presence of particle-like background features in background-suppressed iSCAT images motivate our application of machine learning to aid in particle detection in iSCAT experiments with complex backgrounds.

#### METHODS

**Experimental Details.** 150  $\mu$ m thick glass coverslips were coated with a LbL film (dry thickness = 60 nm, wet thickness = 85 nm) composed of 11 alternating polycation [poly (allylamine hydrochloride)] and polyanion [poly(acrylic acid)] layers. The LbL film was capped by the polycation leaving a positive zeta potential of +14.7 mV on the substrate when exposed to 1 mM sodium phosphate buffer at a pH of 7.0 (see Section S1 for material information and Section S2 for substrate preparation and characterization). LbL films were characterized using atomic force microscopy (AFM, Figures S3 and S4) and shown to increase the roughness of the substrate by a factor of 4 when compared to uncoated glass coverslips used in other iSCAT experiments ( $R_{\rm rms,LBL}$  = 3.2 nm,  $R_{\rm rms,glass}$  = 0.8 nm, area = 10  $\mu$ m × 10  $\mu$ m).

Using a flow cell (Figure S5), a 200 pM solution of monodisperse gold nanoparticles (AuNPs. See Section S4 for solution preparation and characterization) with a mean diameter of 19.2 nm in 1 mM sodium phosphate buffer, pH of 7.0, was exposed to the LbL film on an inverted iSCAT microscope (see Section S5 for iSCAT instrumentation and imaging details). At this pH, the AuNPs had a negative zeta potential of -58 mV because of their carboxy-terminated ligands, and electrostatic interactions drove irreversible adsorption of the AuNPs to the positively charged LbL coated glass coverslip over the course of a 4 h experiment. At 30 min intervals, iSCAT images were collected for ~1 min at a frame rate of 184 fps (~5.44 ms between frames). The pixel size of the iSCAT setup was measured using a stage micrometer to be 50 nm/pixel, giving the 256 × 256 pixel images a field of view of 12.8  $\mu$ m × 12.8  $\mu$ m. This resulted in an experimental dataset consisting of 108 videos of 1000 frames each for a total of 108,000 iSCAT images.

Image Flattening. Raw iSCAT videos were processed in two operations: flattening followed by ratiometric processing. The flattening techniques described here were detailed previously<sup>28</sup> and implemented using custom Python scripts. In the first flattening step, a static background image was collected by laterally translating the sample stage during data collection in a Lissajous pattern using piezoelectric motors and calculated as the pixelwise median of 100 images collected during that movement. Each raw iSCAT image was divided by its corresponding static background image to remove spurious features inherent to the optical configuration. Next, a medianfiltered image containing only features larger than the scattering features of the nanoparticles was calculated by convoluting the image from the first flattening step with a kernel of 21 pixels and calculating the median of pixels in that kernel. The resulting image from the first flattening step was then divided by the median-filtered image yielding flattened images with a mean background value of 1. All subsequent ratiometric processing was done on these flattened images. An example of the conversion of a raw iSCAT image to a flattened image is shown in Figure S7.

**Ratiometric Processing.** After flattening, we employed ratiometric processing <sup>12</sup> to suppress the background. By balancing images that follow a nanoparticle adsorption event with those that precede the event, ratiometric processing

capitalizes on time-dependent variations in scattering signals during the collection of iSCAT videos to isolate adsorption events in background-suppressed images. In doing so, it enables the measurement of the scattering contrast and the binding times of analytes and has been previously used to detect nanoparticles<sup>13</sup> and proteins.<sup>11</sup>

To apply ratiometric processing to detect nanoparticle adsorption events, we began by defining a time-binning window of  $N_{\rm ratio}=5$  frames.  $N_{\rm ratio}$  effectively defined the minimum residence time for a particle to be considered adsorbed as a particle that remained attached to the surface for at least  $2N_{\rm ratio}$  frames. In our experiments,  $N_{\rm ratio}=5$  frames defined the minimum residence to be  $2N_{\rm ratio}\times$  frame interval or 54.3 ms. Faster frame intervals would have allowed for the analysis of shorter residence times, but in our experiments, we did not see any desorption events, indicating that this minimum residence time was sufficient.

We calculated ratiometric images as follows: For a given frame i, two batches of sequential images were averaged to produce two images  $I_1(i)$  and  $I_2(i)$ , where  $I_1(i)$  corresponded to the pixelwise average of images i to  $N_{\text{ratio}}$  and  $I_2(i)$  to images  $i + 1 + N_{\text{ratio}}$  to  $2N_{\text{ratio}}$ . After normalizing  $I_2(i)$  and  $I_1(i)$  by dividing each average image by its mean, we then divided  $\hat{I}_2$ (i)/  $\hat{I}_{l}(i)$  to obtain ratiometric images,  $I_{ratio}(i)$ . Frames were then incremented across each video one frame at a time, creating a new movie consisting of ratiometric images. As frames are incremented forward in time, the scattering contrast of adsorbing particles increases in magnitude reaching a maximum when the adsorption event is located between the two frame batches and decreases back to the background value of 1 thereafter. Adsorption events in our configuration destructively interfered with the reflected light and were manifested in dark spots on a gray background. The reverse process, desorption, if present, would present as bright spots on a gray background. In this way, by finding the point of maximum scattering contrast magnitude, the scattering contrast and occurrence time for adsorption and desorption events can be precisely quantified. An illustration of ratiometric processing is illustrated in Figure S8a-c.

Particle Detection Using the Haar Method. Following ratiometric processing, particle signals or point spread functions (PSFs) were detected using traditional and machine learning object detection algorithms. The Haar-like feature algorithm was implemented in Python following details described in refs 11 and 30. First, ratiometric images were convoluted with a 2D Gaussian in eq 4

$$I_{PSF}(x, y) = A \exp\left(-\left(\frac{(x - x_0)^2}{2\sigma^2} + \frac{(y - y_0)^2}{2\sigma^2}\right)\right) + B$$
 (4)

where A is the contrast amplitude,  $x_0$  and  $y_0$  are the center position, B is the background, and  $\sigma$  is the standard deviation. The parameters of the 2D Gaussian used for the convolution were determined empirically by fitting a particle PSF in a ratiometric image. Next, Haar feature scores were calculated for each pixel with higher scores corresponding to vertical edges, horizontal edges, and circular features using three kernels each  $9 \times 9$  pixels in size. The pixelwise Haar scores were averaged between these three features and weakly thresholded to remove pixels with Haar feature scores lower than 0.20. From the weakly thresholded images, only thresholded pixels with 4 neighbors were kept as candidate

pixels that belong to a particle signal. The probability that a pixel belongs to a particle was then calculated as the fraction of pixels that satisfied all threshold and neighbor candidacy requirements within a  $7 \times 7$  kernel of neighboring pixels. If this probability was greater than 0.3, the pixel was classified as belonging to a particle, resulting in a segmented binary image that was then labeled in object detection. Although the Haarlike feature algorithm was used as a control in this study, it would be valuable in future studies to test other state-of-the-art object detection methods, such as the circular Hough transform used by Melo<sup>13</sup> et al., to see how performance compares to that of the mask R-CNN when the background scattering is high.

Particle Detection Using the Mask R-CNN. The mask R-CNN, described in detail by He<sup>20</sup> et al., detects objects in images in four main stages. First, features are detected and mapped to pixels using a CNN. From these feature maps, bounding boxes around regions of interest (ROIs) are proposed. Then, simultaneously, bounding boxes around ROIs are refined, regions are classified, and instance-level segmentation masks within the refined bounding boxes are generated as the final outputs. In our implementation, we capitalized on the inference output of bounding boxes and classifications to perform Gaussian fitting and particle tracking in subsequent steps.

To implement the mask R-CNN for object detection in iSCAT images, Matterport's implementation<sup>23</sup> of the mask R-CNN in TensorFlow and Keras was used with minor hyperparameter modifications. Namely, a ResNet50 backbone was used, and image dimensions were constrained to the size of our iSCAT images, 256 × 256 pixels. For training, all ROIs with a detection confidence below 0.7 were rejected. In inference, all ROIs with a detection confidence below 0.9 were rejected. We normalized all input images by rescaling their intensity to a minimum of 0 and a maximum of 1 and converted the normalized grayscale images to 8 bit redgreen-blue images. While not an exhaustive optimization, only these minor changes were required to obtain good performance in both training and inference. Additionally, maintaining most hyperparameters at their default values made transfer learning from ImageNet weights easier, reducing the amount of data required for training and shortening the training time on limited computational resources.

Creating Datasets to Train the Mask R-CNN. An essential contribution of this work is the methodology for creating labeled image datasets with realistic experimental backgrounds to use in training a neural network for object detection. A custom Python script was used to generate 500 synthetic dataset images. First, a particle image was generated using a PSF approximation in the form of a 2D Gaussian (eq 4) to generate synthetic nanoparticle signals approximating those measured in iSCAT on an image with a background of 0. In experiments with less background roughness, secondary interference fringes beyond the central lobe maybe visible, and Bessel functions, which more accurately approximate the interference of a plane wave with a spherical wave, may serve as better PSF models for simulated particle signals. PSF parameters (listed in Table 1) were empirically determined by fitting 10 particles from ratiometric images. Notably, an amplitude (A) at the high end of the measured scattering contrast from our experiments was selected to increase the contrast between synthetic particle signals and background features. We found this contrast to be vital to ensure good

Table 1. Parameters Used to Create Synthetic Particle Images for Our Dataset

parameter	value
A (au)	0.06
$\sigma$ (pixels)	2.00
particles per image	10-15
minimum spacing between particles (pixels)	40
minimum particle centroid distance to border (pixels)	5
mask diameter (pixels)	21
particle classes	dark, bright
$\sigma_{ m shot\ noise}\ ( m au)$	0.001-0.004
training image number	350
test image number	150

performance during inference. Dark particles were assigned a negative amplitude, while bright particles were assigned a positive amplitude in the 2D Gaussian. Particles were randomly positioned within an image of the same size as the iSCAT ratiometric images with the minimum spacing between other particles and the border limited, and positions and particle class types were logged. Instance-level masks with corresponding class labels were then generated using particle positions and a circular mask of defined size to serve as the ground truth in training.

To add variance to the dataset and make it more realistic, a shot noise image of Gaussian noise with a mean of 0 and a given standard deviation,  $\sigma_{
m shot\ noise}$ , was created. Next, a real background from the ratiometric experimental images was sampled as follows: One image from every third video (1,4,7,...,106) in the experiment was randomly selected to capture representations of the background over the course of the iSCAT experiment. To ensure that background images contain no particles, images were visually inspected and resampled until no particle PSFs were present in any background images resulting in a set of 36 particle-free ratiometric background images. When the dataset was generated, one image from this set was randomly selected to serve as the background for that image. Figure 1 shows how the particle image, shot noise, and randomly sampled background (top row) were summed to create the dataset image (bottom, left) and corresponding labels for each class (bottom, middle, and right).

Training the Mask R-CNN. Training via transfer learning was implemented using configurations detailed by Abdulla<sup>22</sup> with minimal modifications. In brief, network weights were initialized from a mask R-CNN trained on the ImageNet dataset. Three new classes ("background", "bright", and "dark") were defined for the generated dataset images and corresponding masks. Images in the dataset were augmented during training through vertical and horizonal flips, Gaussian blurring, and scaling to limit overfitting and improve generalization. Head weights were fine tuned for the first 20 epochs of training at a learning rate of 0.001 followed by fine tuning of all network weights at a learning rate of 0.0001 for a total of 200 training epochs. Trained model weights were saved after each epoch. The loss function decayed, and average precision increased (Figure S9) in both training and validation, indicating that the mask R-CNN learned iSCAT particle signals and showed no signs of overfitting. Visual inspection of the performance of the mask R-CNN (Figure S10) confirmed that the mask R-CNN learned particle signals successfully. On a standard desktop computer (8 GB 2070 NVIDIA RTX GPU,

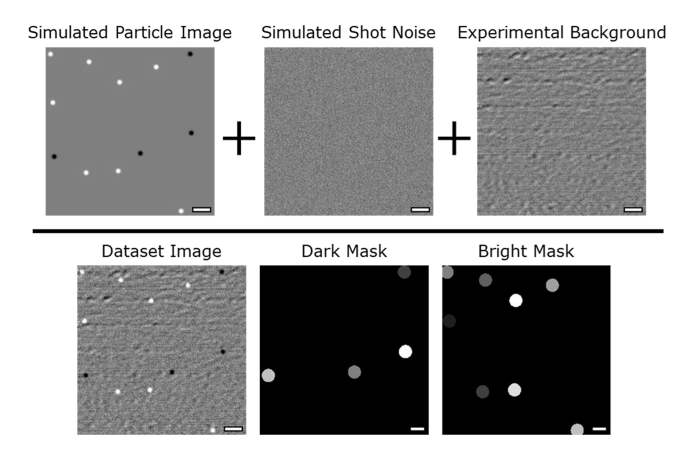


Figure 1. Visual representation of the process of creating labeled datasets for training the mask R-CNN via transfer learning. The dataset image (bottom, left) was created by summing the simulated particle image (containing randomly positioned synthetic PSFs), a simulated shot noise image, and a randomly sampled experimental ratiometric background image. Using stored particle positions from the simulated particle image, instance-level masks (bottom, middle, and right) for dark and bright particle classes served as labels for training and testing. All scale bars are 1  $\mu \rm m$  but were not included in the dataset images.

AMD Ryzen 5 2600X 6 Core CPU, 64 MB RAM), training on the 500-image synthetic dataset was completed in  $\sim$ 40 min. Inference predictions of particle detection by the mask R-CNN on experimental iSCAT data were inspected visually using weights from the 100th and 200th epochs. The 200th epoch showed the best performance despite a plateau in precision during training and validation after  $\sim$ 50 epochs. We hypothesize that this extended training beyond average precision saturation allowed for enhanced learning of the background and thus justified the use of weights from the 200th epoch in all subsequent analyses.

Single Particle Tracking. From PSFs detected in ratiometric images, the magnitude of the scattering contrast and event time for an adsorbing or desorbing particle were quantified using single particle tracking techniques. First, PSFs from adsorption events were detected using the Haar or mask R-CNN methods. For detections using the Haar method, bounding boxes of 15 pixels around the centroids of the proposed particle detections were generated. For detections using the mask-RCNN, bounding boxes from inference were directly used. Any candidate particle with a bounding box center within 5 pixels of the image border was discarded. The PSFs of candidate particles were fit to a 2D Gaussian<sup>31</sup> using a least-squares regression algorithm from the LMFIT<sup>32</sup> Python package using eq 4 where contrast amplitude, A, and center position  $(x_0, y_0)$  of the Gaussian were allowed to vary, while the background, B, and standard deviation,  $\sigma$ , were fixed at 1.0 contrast units and 2.0 pixels (~100 nm), respectively. Fixed values were determined by empirical fits to PSFs manually sampled from ratiometric images. In Haar detections, the signal to noise ratio, SNR, for each proposed detection was calculated as the ratio of |A| to the background standard deviation, and all detections with an SNR less than 3 were discarded. The A, frame, time, and position for all PSFs were logged. After PSF detection and fitting, PSFs with center positions within 2 pixels of each other in subsequent ratiometric images for a minimum of 6 frames were linked into trajectories using the Trackpy Python package.<sup>33</sup> Within

each trajectory, the average of the two highest magnitude amplitude (|A|) points was used to separate the data for a given particle trajectory into regions of the opposite slope. Two lines were fit to A as a function of time in each region, and the position of intersection of these lines was defined as the relative scattering contrast,  $|A_{\rm event}|$ , and event time at sub-frame interval temporal resolution. We note that for convenience,  $|A_{\rm event}|$  will be referred to as scattering contrast for the remainder of this work. An example of the single particle tracking techniques used to quantify the scattering contrasts and event times of an adsorption event is illustrated in Figure S8d,e.

#### RESULTS

**Stage Vibrations Lead to FPs.** The LbL films used in the model experiment analyzed here exhibited higher roughness compared to minimally functionalized glass coverslips used in other iSCAT experiments (AFM images in Figures S3 and S4,  $R_{\rm rms,LbL} = 3.2$  nm,  $R_{\rm rms,glass} = 0.8$  nm, area =  $10~\mu{\rm m} \times 10~\mu{\rm m}$ ). Figure 2 shows that when the LbL film roughness was coupled

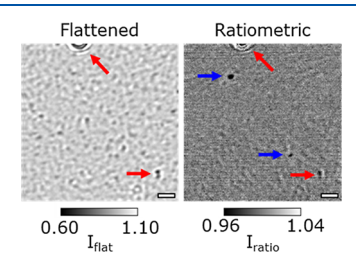
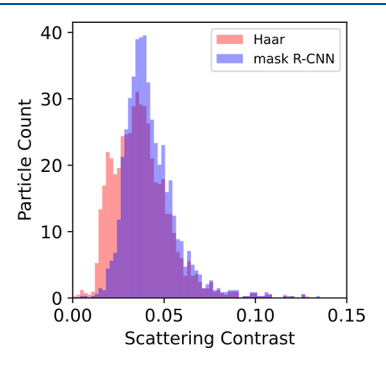


Figure 2. (Left) flattened image from an iSCAT experiment of 19.2 nm AuNPs adsorbing to LbL films with 3.2 nm roughness. Increased substrate roughness created regions of high scattering contrast, indicated by the red arrows. Scattering from the background dominated the image, and particle signatures were indistinguishable from the background. (Right) ratiometric image from the same experiment. Stage movements caused strongly scattering roughness features to show up in the background of the ratiometric images as indicated by the red arrows. These background features have similar contrast and morphologies to the scattering features from AuNPs as indicated by the blue arrows. All scale bars are 1  $\mu m$ .

with stage movements, strong scattering features (red arrows, left) were manifested as particle-like features in ratiometric images (red arrows, right). These background features had contrasts and morphologies similar to those of the AuNP scattering signals (blue arrows, right). The Haar method used to detect particles frequently identified these features as particles leading to FP identifications. In this way, Figure 2 highlights the limitations of using edge and threshold-based image analysis algorithms, such as the Haar method, to detect particles.

Reducing FP Detections with the Mask R-CNN. CNNs have been shown to be successful in object detection and to be less sensitive to algorithm parameters that normally must be tuned for object detection in every experiment. To see if these benefits translate to iSCAT image processing, a hybrid dataset containing background images from an iSCAT experiment and simulated particle PSFs was generated as described in the Methods section. This dataset was used to fine tune mask R-CNN weights via transfer learning, giving a CNN adept at identifying and classifying common place objects (e.g., animals, balls) and the ability to identify and classify nanoparticle PSFs in ratiometric iSCAT images. We compare

the performance of particle detection using the mask R-CNN with that of the Haar method by analyzing the data from the same AuNP-LbL adsorption experiment using both methods in Figure 3.



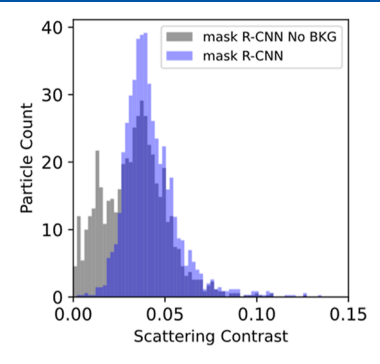
**Figure 3.** Histograms of scattering contrast for particles detected using the Haar method (pink) and mask R-CNN (blue). Scattering contrast ( $|A_{\text{event}}|$ ) represents the peak contrast amplitude for each particle as determined by the single particle tracking algorithm.

Figure 3 shows the distribution of scattering contrasts measured using ratiometric image processing and detected using the Haar method (pink) and mask R-CNN (blue). In the mask R-CNN histogram, the distribution is monomodal with a peak at ~0.04. The Haar histogram is bimodal, with a dominant peak at  $\sim$ 0.04 and a second lower peak at  $\sim$ 0.02 (the peak position and count were determined by eye). The bimodal nature of scattering contrasts detected by the Haar method demonstrates the main improvement in performance of the mask R-CNN over the Haar method. Despite our particles being monodisperse in size (as confimed by the SEM image shown in Figure S6), the Haar histogram shows multiple peaks in ratiometric scattering contrast. The low contrast peak near 0.02 in the Haar histogram, indicative of FPs during particle detection, is not present in the mask R-CNN histogram. Moreover, the breadth of the low-scattering intensity peak near 0.02 in the Haar histogram overlaps significantly with the breadth of the central peak in the Haar histogram at 0.04. Because of this overlap, post-processing to remove FP detections without excluding true positive (TP) detections was not feasible. In addition, mask R-CNN's detection capabilities are invariant to parameter settings such as the minimum SNR (Figure S11), while the Haar algorithm is very sensitive to the minimum SNR value, leading to improved trajectory linking during particle tracking. This invariance also emphasizes the ability of the mask R-CNN to identity particles in complex backgrounds at low SNR values. Also, though beyond the scope of this work, the ability to detect objects at low SNRs would extend the capability of iSCAT experiments to detect weaker scattering objects such as proteins or small, low-dielectric nanoparticles in complex, heterogeneous backgrounds as has been recently shown by Dahmardeh et al.<sup>34</sup> in a publication currently under review.

Learning the Background Improves Performance with the Mask R-CNN. The ability of CNNs to detect objects has been attributed to the ability of the network to learn features related to the objects of interest. However, CNNs also inherently learn to classify features as belonging to the background. The overlap of the dominant peaks at 0.04 in both histograms shown in Figure 3 suggests that detecting particles is not the main challenge, but rather, the problem lies

in discerning particles from the background—the inverse problem in object detection. Also, because there is no bimodal behavior in the mask R-CNN histogram due to FP detections at low scattering contrasts, the improved performance of the mask R-CNN may not stem from an ability to learn a better representation of the particle signals but instead its ability to learn a better representation of the background in iSCAT ratiometric images. Therefore, the inclusion of representative background images that capture real experimental backgrounds in datasets for training may be important.

To test the hypothesis that including experimentally representative backgrounds in the dataset improves mask R-CNN's performance relative to edge detection and threshold based methods like the Haar-method, an analogous dataset was generated without the inclusion of representative background images from ratiometric images. Figure 4 presents histograms of the scattering contrast detected by mask R-CNNs trained with (blue) and without (gray) experimental backgrounds in the dataset images.



**Figure 4.** Histograms of scattering contrast comparing the performance of mask R-CNN models trained on datasets that included (blue) and did not include (gray) experimental backgrounds. Scattering contrast ( $|A_{\text{event}}|$ ) represents the peak contrast amplitude for each particle as determined by the single particle tracking algorithm.

Figure 4 demonstrates the impact of including representative experimental backgrounds in the training dataset. An increased density of FP detections appears at scattering contrast values centered around 0.01 when particle detection is executed with the mask R-CNN trained on a dataset that did not include information about the background. The central scattering peak at 0.04 was also slightly decreased in the particle count when data was processed using the mask R-CNN trained on the dataset that did not contain experimental backgrounds (the peak position and count were again determined by eye). This indicates that in addition to reducing FPs, insufficient learning of background features may result in missed detections. Consequently, the improved performance of the mask R-CNN is not solely a product of learning of the background features. Rather, it is a combination of the ability of the mask R-CNN to learn the background and to better detect particle features in that background when the mask R-CNN is exposed to experimental backgrounds during training.

#### DISCUSSION

#### Visual Inspection of 100 Randomly Selected Images.

To quantify the performance of the Haar method against that of both mask R-CNN models (trained using datasets with and without background), 100 random images were selected from the experimental ratiometric images. For each image, the three

object detection methods described in the Results section were used to detect particles in the same sampled image, and the results were inspected visually to assess performance by counting the number of TP, FP, and false negative (FN) detections. Examples of true and FP detections are shown in Figure 2. FNs are particle signals that have not been detected by the algorithm as potential PSFs. From this, precision and recall were calculated, and the results are tabulated in Table 2.

Table 2. Summary of Results of Particle Detection in 100 Randomly Selected iSCAT Images Analyzed by Visual Inspection across the Three Methods Tested

	Haar	mask R-CNN (no background)	mask R-CNN (with background)
total particles (ground truth)	81	81	81
TP count	77	68	79
FP count	19	21	3
FN count	4	13	2
precision <sup>a</sup>	80.2%	76.4%	96.3%
recall <sup>b</sup>	95.1%	84.0%	97.5%

<sup>&</sup>lt;sup>a</sup>Precision is defined as TP/(TP + FP). <sup>b</sup>Recall is defined as TP/(TP + FN).

We note that true negative detections cannot be quantified in object detection tasks as there are an infinite number of pixel groupings that form background features that should not be detected.<sup>36</sup> Due to the low concentration of particles in solution, landing events occurred infrequently during our experiment, resulting in ratiometric images that contained 0–2 particles on average.

Table 2 summarizes the results of the visual inspection of 100 random images. The biggest difference in performance across the three methods is seen in the FP count where the Haar, mask R-CNN (no background), and mask R-CNN methods incorrectly identified 19, 21, and 3 background features as particle PSFs, respectively. In general, the numbers given in Table 2 agree with the distributions of scattering contrast shown in Figures 3 and 4 and support the observation that the secondary, low-scattering contrast peaks at 0.010 represent FPs and have the biggest impact on the quality of PSF detection in these iSCAT images.

In Table 2, we also quantified performance using precision and recall metrics. Recall quantifies the ability of each method to capture all possible PSF-like features without missing features that represent true particle PSFs. Precision quantifies the accuracy of those detections and thus quantifies the impact of FPs on the analysis. An optimal particle detection algorithm would detect all features that represent particle PSFs (high recall) without incorrectly identifying background features as particle PSFs (high precision). The Haar method recall is 95.1%, indicating that the Haar method detects particles well, but precision is 80.2% as many background features are identified as particle signals. In the mask R-CNN (no background) method, both recall (76.4%) and precision (84.0%) are lower than those in the Haar method indicating that without the background in the training datasets, the neural network suffers from falsely detecting background features as particle signals and from missing real particle signals when they are convoluted with the background. We see the best performance in the mask R-CNN (with background) where high recall (97.5%) and precision (96.3%) show that the mask

R-CNN, when trained using a dataset that includes experimental backgrounds, correctly identifies particle PSFs while also correctly avoiding classifying background features as particles. Evidently, neural networks demonstrate the potential to learn experimental backgrounds, and this translates to improved performance in particle detection in iSCAT experiments.

FP Detections Negatively Impact Single Particle **Tracking.** The analysis described in the Methods section utilized single particle tracking algorithms to link PSFs detected into trajectories based on the proximity of the PSF centroid locations in subsequent ratiometric images. We then used these trajectories to fit lines to the PSF amplitude versus time. When a feature representing an adsorbing particle in a ratiometric video was correctly identified, the trend of scattering contrast with time within a trajectory followed a linear decrease to the time of the adsorption event followed by a linear increase after the adsorption event as shown in the example in Figure S8e. However, when FP detections of the background features are present, particle tracking algorithms may link a true particle detection with an FP if the false position is close to the TP position from the previous image. When this happens, the trends in A with time for a given trajectory can deviate from the expected decreasing-increasing pattern, and this causes the linear fit algorithm to either fail or report an incorrect scattering contrast and adsorption event time. In general particle tracking experiments, such as those that measure diffusion, incorrect linking can skew the detected velocity.<sup>37</sup> Thus, the improvements in particle detection demonstrated here could benefit all particle tracking studies, and our dataset creation/training methodology provides a single particle tracking strategy with improved reliability.

Utility Beyond iSCAT. The main contribution here is the methodology behind including real experimental background images in datasets for training CNNs via supervised machine learning. Including real background images in the training datasets leads to an improvement in particle detection and, more importantly, a reduction in FPs when iSCAT images are analyzed with the mask R-CNN. However, the process developed here is not limited to iSCAT experiments. If experimentalists can accurately capture the background in their collected images and model signals (e.g., PSFs) that they wish to detect, they can create labeled datasets for many types of experimental images (e.g., AFM, transmission and scanning electron microscopy, and other optical microcopy methods) to aid in the development of accurate, high-throughput processing of their data using machine learning without the need for expensive, high-performance computing resources.

A particular challenge for further expansion of the methods for creating labeled datasets that include experimental backgrounds described here is that it requires a researcher to have access to background images lacking the target objects of interest. Dataset creation in this work was enabled by the low (200 pM) concentration nanoparticle solutions used in our adsorption experiment. The low concentration of nanoparticles slowed the adsorption process relative to the frame rate of iSCAT (184 fps) to the point that only 0–2 events were detected per frame and resulted in multiple ratiometric images that contained no particle signatures. For characterization tools compatible with solutions such as iSCAT, a blank solution could also have been imaged without particles. This situation, though, is inefficient from a data versus information standpoint and is uncommon in other characterization methods. To

implement the dataset creation method in experiments where all images contain objects of interest, users would need to remove the objects from their images to create signal-free background images, which requires detecting them, rendering the workflow obsolete. A promising approach to extend the method of creating datasets with real experimental backgrounds may exist in the computer vision machine learning field in the form of neural style transfer.<sup>38</sup> In neural style transfer, a neural network takes two images as inputs, a content image and a style reference, and blends the two together such that the output image contains important features in the content image "painted" in the style of the reference image. In our workflow, the content image would be the particle image shown in Figure 1, and the reference would be sets of images from an experiment with or without particles (i.e., the experimental ratiometric background image shown in Figure 1). In theory, the output from this network could result in a dataset containing synthetic particles in an image atop a realistic background with labels from the particle image serving as ground truth labels for training.

#### CONCLUSIONS

The methods presented here demonstrate a workflow for creating labeled datasets with representative experimental backgrounds containing simulated particle signals on background-suppressed iSCAT microscopy images to use in training a mask R-CNN using transfer learning without extensive computational resources. Results showed that the high performance of the mask R-CNN in detecting nanoparticles adsorbing to a rough, high-scattering LbL film in an iSCAT experiment stemmed from the ability of the mask R-CNN to learn background features, thereby reducing the number of FP detections. The improved analysis technique expands capability of iSCAT to detect scattering objects in situations where background scattering is complex.

#### ■ ASSOCIATED CONTENT

#### **Supporting Information**

The Supporting Information is available free of charge at https://pubs.acs.org/doi/10.1021/acs.jpcb.3c00097.

Details regarding image flattening, ratiometric processing, mask R-CNN training, iSCAT instrumentation and flow cells, materials, substrate preparation, substrate characterization, and gold nanoparticle characterization (PDF)

#### AUTHOR INFORMATION

#### **Corresponding Author**

Russell J. Composto – Department of Materials Science and Engineering, University of Pennsylvania, Philadelphia, Pennsylvania 19104, United States; oorcid.org/0000-0002-5906-2594; Email: composto@seas.upenn.edu

#### **Authors**

Michael J. Boyle — Department of Materials Science and Engineering, University of Pennsylvania, Philadelphia, Pennsylvania 19104, United States; Center for Engineered Materials and Manufacturing, Lawrence Livermore National Laboratory, Livermore, California 94550, United States; orcid.org/0000-0001-7010-3820

Yale E. Goldman – Department of Physiology and Pennsylvania Muscle Institute, University of Pennsylvania,

Philadelphia, Pennsylvania 19104, United States; orcid.org/0000-0002-2492-9194

Complete contact information is available at: https://pubs.acs.org/10.1021/acs.jpcb.3c00097

#### Notes

The authors declare no competing financial interest.

#### ACKNOWLEDGMENTS

We thank the National Science Foundation (NSF) Graduate Research Fellowships Program (GRFP); NSF Chemical, Bioengineering, Environmental, and Transport Systems (CBET) 2034122; National Institutes of Health (NIH) R35GM118139; NSF Division of Materials Research (DMR) Polymers Program DMR1905912; NSF Partnerships for International Research; the Center for Engineering MechanoBiology NSF Science and Technology Center, CMMI: 15-48571; and the Education for the Office of International Science and Engineering PIRE-OISE-1545884 that provided support for this work. This work also was carried out in part at the Singh Center for Nanotechnology, which is supported by the NSF National Nanotechnology Coordinated Infrastructure Program under grant NNCI-2025608. This work was performed in part under the auspices of the U.S. Department of Energy by Lawrence Livermore National Laboratory under contracts DE-AC52-07NA27344 and IM LLNL-JRNL-842942. Lastly, we thank Drs. Nathan Frey, James Horwath, and Chris Price for discussions regarding the implemented machine learning methods; Gautam Jain for AFM images; Drs. Daeyeon Lee and Wilfredo Mendez Ortiz for assistance in preparing LbL films; Dr. Matthew Capporizzo for assistance in operating the iSCAT equipment; and Drs. Jan Genzer and Yeongun Ko at North Carolina State University for fruitful discussions.

#### REFERENCES

- (1) Taylor, R. W.; Sandoghdar, V. Interferometric Scattering (ISCAT) Microscopy and Related Techniques. In *Label-Free Super-Resolution Microscopy*; Astratov, V., Ed.; Springer International Publishing: Cham, 2019, pp 25–65.10.1007/978-3-030-21722-8\_2.
- (2) Strack, R. Scattering Microscopy Takes Single-Particle Tracking to the next Level. *Nat. Methods* **2019**, *16*, 455.
- (3) Holanová, K.; Vala, M.; Piliarik, M. [INVITED] Optical imaging and localization of prospective scattering labels smaller than a single protein. *Opt Laser. Technol.* **2019**, *109*, 323–327.
- (4) Jacobsen, V.; Stoller, P.; Brunner, C.; Vogel, V.; Sandoghdar, V. Interferometric Optical Detection and Tracking of Very Small Gold Nanoparticles at a Water-Glass Interface. *Opt. Express* **2006**, *14*, 405.
- (5) Spindler, S.; Ehrig, J.; König, K.; Nowak, T.; Piliarik, M.; Stein, H. E.; Taylor, R. W.; Garanger, E.; Lecommandoux, S.; Alves, I. D.; et al. Visualization of Lipids and Proteins at High Spatial and Temporal Resolution via Interferometric Scattering (ISCAT) Microscopy. J. Phys. D Appl. Phys. 2016, 49, 274002.
- (6) Kukura, P.; Ewers, H.; Müller, C.; Renn, A.; Helenius, A.; Sandoghdar, V. High-Speed Nanoscopic Tracking of the Position and Orientation of a Single Virus. *Nat. Methods* **2009**, *6*, 923–927.
- (7) Heermann, T.; Steiert, F.; Ramm, B.; Hundt, N.; Schwille, P. Mass-Sensitive Particle Tracking to Elucidate the Membrane-Associated MinDE Reaction Cycle. *Nat. Methods* **2021**, *18*, 1239–1246
- (8) Foley, E. D. B.; Kushwah, M. S.; Young, G.; Kukura, P. Mass Photometry Enables Label-Free Tracking and Mass Measurement of Single Proteins on Lipid Bilayers. *Nat. Methods* **2021**, *18*, 1247–1252.
- (9) Ortega Arroyo, J.; Andrecka, J.; Spillane, K. M.; Billington, N.; Takagi, Y.; Sellers, J. R.; Kukura, P. Label-Free, All-Optical Detection,

Imaging, and Tracking of a Single Protein. Nano Lett. 2014, 14, 2065–2070.

- (10) Andrecka, J.; Takagi, Y.; Mickolajczyk, K. J.; Lippert, L. G.; Sellers, J. R.; Hancock, W. O.; Goldman, Y. E.; Kukura, P. Interferometric Scattering Microscopy for the Study of Molecular Motors, in *Methods in Ezymology*, 1st ed.; Elsevier Inc., 2016; Vol. 581. DOI: 10.1016/bs.mie.2016.08.016.
- (11) Young, G.; Hundt, N.; Cole, D.; Fineberg, A.; Andrecka, J.; Tyler, A.; Olerinyova, A.; Ansari, A.; Marklund, E. G.; Collier, M. P.; et al. Quantitative Mass Imaging of Single Biological Macromolecules. *Science* **2018**, *360*, 423–427.
- (12) Cole, D.; Young, G.; Weigel, A.; Sebesta, A.; Kukura, P. Label-Free Single-Molecule Imaging with Numerical-Aperture-Shaped Interferometric Scattering Microscopy. *ACS Photonics* **2017**, *4*, 211–216.
- (13) Melo, L.; Hui, A.; Kowal, M.; Boateng, E.; Poursorkh, Z.; Rocheron, E.; Wong, J.; Christy, A.; Grant, E. Size Distributions of Gold Nanoparticles in Solution Measured by Single-Particle Mass Photometry. J. Phys. Chem. B 2021, 125, 12466–12475.
- (14) Ortega Arroyo, J.; Cole, D.; Kukura, P. Interferometric Scattering Microscopy and Its Combination with Single-Molecule Fluorescence Imaging. *Nat. Protoc.* **2016**, *11*, 617–633.
- (15) Taylor, R. W.; Sandoghdar, V. Interferometric Scattering Microscopy: Seeing Single Nanoparticles and Molecules via Rayleigh Scattering. *Nano Lett.* **2019**, *19*, 4827–4835.
- (16) Strack, R. ISCAT Gets a Signal Boost. Nat. Methods 2021, 18, 447.
- (17) Liebel, M.; Hugall, J. T.; Van Hulst, N. F. Ultrasensitive Label-Free Nanosensing and High-Speed Tracking of Single Proteins. *Nano Lett.* **2017**, *17*, 1277–1281.
- (18) Cheng, C. Y.; Hsieh, C. L. Background Estimation and Correction for High-Precision Localization Microscopy. *ACS Photonics* **2017**, *4*, 1730–1739.
- (19) Chatzidakis, M.; Botton, G. A. Towards Calibration-Invariant Spectroscopy Using Deep Learning. Sci. Rep. 2019, 9, 2126.
- (20) He, K.; Gkioxari, G.; Dollar, P.; Girshick, R. Mask R-CNN. IEEE Trans. Pattern Anal. Mach. Intell. 2020, 42, 386–397.
- (21) Horwath, J. P.; Zakharov, D. N.; Mégret, R.; Stach, E. A. Understanding Important Features of Deep Learning Models for Segmentation of High-Resolution Transmission Electron Microscopy Images. *npj Comput. Mater.* **2020**, *6*, 108.
- (22) Frei, M. .; Kruis, F. E. Image-Based Analysis of Dense Particle Mixtures via Mask R-CNN. *Eng* **2022**, *3*, 78–98.
- (23) Abdulla, W. Mask R-CNN for Object Detection and Instance Segmentation on Keras and TensorFlow. GitHub repository; Github, 2017.
- (24) Panigrahi, S.; Nanda, A.; Swarnkar, T. A Survey on Transfer Learning. Smart Innov. Syst. Technol. 2021, 194, 781–789.
- (25) Yang, L.; Parton, R.; Ball, G.; Qiu, Z.; Greenaway, A. H.; Davis, I.; Lu, W. An Adaptive Non-Local Means Filter for Denoising Live-Cell Images and Improving Particle Detection. *J. Struct. Biol.* **2010**, 172, 233–243.
- (26) Young, G.; Kukura, P. Interferometric Scattering Microscopy. *Annu. Rev. Phys. Chem.* **2019**, *70*, 301–322.
- (27) Ortega-Arroyo, J.; Kukura, P. Interferometric Scattering Microscopy (ISCAT): New Frontiers in Ultrafast and Ultrasensitive Optical Microscopy. *Phys. Chem. Chem. Phys.* **2012**, *14*, 15625–15636.
- (28) Ortega Arroyo, J.; Cole, D.; Kukura, P. Interferometric Scattering Microscopy and Its Combination with Single-Molecule Fluorescence Imaging. *Nat. Protoc.* **2016**, *11*, 617–633.
- (29) Sources of vibration. https://www.thorlabs.com/tutorials/Tables2.cfm. (accessed June 28, 2022).
- (30) Lu, Y. Y.; Noble, W. S. A wider field of view to predict expression. *Nat. Methods* **2021**, *18*, 1155–1156.
- (31) Shen, H.; Tauzin, L. J.; Baiyasi, R.; Wang, W.; Moringo, N.; Shuang, B.; Landes, C. F. Single Particle Tracking: From Theory to Biophysical Applications. *Chem. Rev.* **2017**, *117*, 7331.

- (32) Newville, M.; Stensitzki, T.; Allen, D. B.; Ingargiola, A. LMFIT: Non-Linear Least-Square Minimization and Curve-Fitting for Python (0.8.0). Zenodo 2014. DOI: 10.5281/zenodo.11813.
- (33) Allan, D. et al. Soft-Matter/Trackpy: Trackpy v0.4.2. Zenodo October 2019. DOI: 10.5281/zenodo.3492186.
- (34) Dahmardeh, M.; Dastjerdi, H. M.; Mazal, H.; Köstler, H.; Sandoghdar, V. Self-Supervised Machine Learning Pushes the Sensitivity Limit in Label-Free Detection of Single Proteins below 10 KDa. *Nat. Methods* **2022**, *20*, 442.
- (35) Newby, J. M.; Schaefer, A. M.; Lee, P. T.; Forest, M. G.; Lai, S. K. Convolutional Neural Networks Automate Detection for Tracking of Submicron-Scale Particles in 2D and 3D. *Proc. Natl. Acad. Sci. U.S.A.* **2018**, *115*, 9026–9031.
- (36) Padilla, R.; Netto, S. L.; da Silva, E. A. B. A Survey on Performance Metrics for Object-Detection Algorithms. In 2020 International Conference on Systems, Signals and Image Processing (IWSSIP); 2020; pp 237-242. DOI: 10.1109/IWS-SIP48289.2020.9145130.
- (37) Rose, K. A.; Molaei, M.; Boyle, M. J.; Lee, D.; Crocker, J. C.; Composto, R. J. Particle Tracking of Nanoparticles in Soft Matter. *J. Appl. Phys.* **2020**, *127*, 191101.
- (38) Gatys, L.; Ecker, A.; Bethge, M. A Neural Algorithm of Artistic Style. J. Vis. 2016, 16, 326.

### ☐ Recommended by ACS

#### Plasmonic Scattering Imaging of Surface-Bonded Nanoparticles at the Solution-Solid Interface

Wen-Li Lv, Xian-Wei Liu, et al.

JUNE 09, 2023

ACS APPLIED MATERIALS & INTERFACES

READ 🗹

## **High Resolution of Plasmonic Resonance Scattering Imaging** with Deep Learning

Ming Ke Song, Jun Zhou, et al.

MARCH 11, 2022

ANALYTICAL CHEMISTRY

READ 🗹

Minimizing the Optical Illusion of Nanoparticles in Single Cells Using Four-Dimensional Cuboid Multiangle Illumination-Based Light-Sheet Super-Resolution Imaging

Yingying Cao, Seong Ho Kang, et al.

DECEMBER 12, 2022

ANALYTICAL CHEMISTRY

READ 🗹

## Disentanglement of Multiple Scattering Contribution in Brillouin Microscopy

Maurizio Mattarelli, Silvia Caponi, et al.

MAY 27, 2022

ACS PHOTONICS

READ 🗹

Get More Suggestions >